SNARE-dependent mitochondria-lysosome contacts regulate glial mitochondrial dynamics and dopaminergic neuron survival

Honglei Wang[1], Linfang Wang[1], Shuanglong Yi[1], Shiping Zhang[1], Margaret S. Ho[1*]

[1]School of Life Science and Technology, ShanghaiTech University, Shanghai, 201210, China

[*]Corresponding author:
Margaret S. Ho, Ph.D.
#B416, L building,
#230 Haike Road, Pudong New District,
Shanghai, 201210
Phone: +86-21-2068-5424
Email: margareth@shanghaitech.edu.cn

Summary

Mitochondria are dynamic organelles that undergo fission and fusion, enabling swift structural modification to adapt cellular needs. Disturbances in mitochondrial dynamics, frequently defects ascribed to neurons, have been associated with pathological contexts such as neurodegeneration in Parkinson's disease. Nonetheless, the mechanism of glial mitochondrial dynamics contributing to neurodegeneration remains unclear. Here we present evidence that the *Drosophila* R-SNARE VAMP7 regulates glial mitochondrial dynamics and dopaminergic neuron survival via modulating the dynamic of mitochondria-lysosome contact, which determines the mitochondrial fission site. Independent of its characterized role in autophagosome-lysosome fusion, glial VAMP7 depletion causes mitochondrial elongation and dysfunction, increased ROS levels, and production of lipid droplets. These conferred changes in glia in turn affects nearby dopaminergic neuron survival. Glial VAMP7 genetically interacts with the mitochondrial fission/fusion factors Drp1 and Marf1 and controls glial mitochondrial dynamics via regulating the frequency and duration of mitochondria-lysosome contact. Our findings indicate that SNARE proteins, although not direct mediators on mitochondrial fusion, provide spatial cues to modulate glial mitochondrial fission via organelle contacts, impacting on neuron survival in a non-cell-autonomous manner.

Keywords

VAMP7; Glia; Mitochondrial Dynamics; Mitochondria-Lysosome Contact;

Neurodegeneration

Introduction

Mitochondria are dynamic organelles that undergo structural and functional changes in response to a variety of cellular signals such as energy production, metabolism, or survival. They constantly remodel and interact with other organelles so that their morphologies are swiftly modified to adapt the cellular needs. Different aspects of mitochondrial dynamics have been uncovered including fission (division), fusion, or shape transition, generating different forms of mitochondria that function in various cellular contexts (1-3). These dynamic changes in morphology and function are under tight regulation and have been extensively linked to catastrophic consequences such as neurodegeneration and death (4, 5). For instance, mitochondrial fission regulated by dynamin-related protein-1 (Drp1), a GTPase that dynamically associates with the endoplasmic reticulum (ER) and mitochondria (6-10), suppresses oxidative damage and safeguards neuron survival (11). It is generally considered that the fission process generates smaller mitochondria easier to be targeted by mitophagy, the autophagosomal degradation of damaged mitochondria mediated by Parkinson's disease (PD) risk genes *PINK1* and Parkin (12-14). On the other hand, elongated mitochondria due to the lack of fission accumulate oxidative damage and lose respiratory function, transforming into large spheres resistant to mitophagy. Interestingly, most of these mitochondrial dynamic defects underlying neurodegeneration are ascribed to neurons, whereas how mitochondrial dynamics in glia, the other major brain cell type important for neuron survival, contributes to

neurodegeneration, remains very limitedly explored.

In addition to ER, mitochondrial fission sites are also contacted by lysosomes, which help to restrict mitochondria motility by recruiting the lysosome GTPase Rab7 (15, 16). It has been shown that Rab7 GTP hydrolysis is crucial for the untethering of lysosome and mitochondria (16). Upon mitochondria-lysosome contact untethers, mitochondrial fission occurs. These findings implicate a role for lysosome in regulating mitochondrial dynamics. In regard to this aspect, whether lysosome and its related factors play a role in glial mitochondrial fission is largely unknown; how mitochondrial dynamic is controlled in glia has not been extensively studied.

The *Drosophila* vesicular R-SNARE (soluble N-ethylmaleimide-sensitive factor attachment protein receptors), VAMP7, is homologous to mammalian VAMP7 and VAMP8, and the latter exhibits a prominent expression in microglia (17, 18). Mammalian VAMP7 or VAMP8 localizes on the late endosome and lysosome and forms a complex with the cytosolic Synaptosomal-associated protein 29 (SNAP-29) and the autophagosomal Syntaxin-17 (Syx17); together this complex regulates the autophagosome-lysosome fusion in autophagy (19, 20). Despite a role in vesicle fusion, whether VAMP7 plays additional roles with respect to its lysosomal origin remains unclear. Here we present evidence that VAMP7 regulates glial mitochondrial dynamics via modulating the dynamics of mitochondria-lysosome contacts. Lack of glial VAMP7 causes mitochondrial elongation independent of its autophagy function, increased ROS levels and the production of lipid droplets (LDs), and regulates nearby dopaminergic (DA) neuron survival. Glial VAMP7-mediated mitochondrial

elongation is suppressed by expressing the fission factor Drp1 or downregulating the expression of the mitochondrial assembly regulatory factor Marf, indicating a role for glial VAMP7 in mitochondrial fission/fusion. Considering that SNARE proteins mediate membrane fusion, our findings uncover a new role for a canonical SNARE factor in glial mitochondrial fission, demonstrating its importance in glial contribution to neuron survival.

Results

Glia deficient of VAMP7 exhibit mitochondrial elongation

Previously characterized as a fusion factor regulating autophagosome-lysosome fusion, we first confirm if VAMP7 functions similarly in glia. Two independent RNAi lines: *vamp7*-RNAi$^{\#38300}$ and *vamp7*-RNAi$^{\#43543}$ were used to selectively silence *vamp7* expression. Expression of either RNAi in glia abolished *vamp7* transcription levels, validating the efficacy of RNAi (Figure S1A). Consistent to previous findings, glial autophagic flux monitored by a dual reporter *UAS-GFP-mCherry-Atg8a* in the absence of glial VAMP7 was strikingly impaired. The values of Pearson's coefficient indicating colocalization of GFP and mCherry fluorescent signals were significantly increased upon glial VAMP depletion, indicating non-quenched GFP signals due to impaired fusion (Figure S1B and S1C). These results confirm a role for VAMP7 in glial autophagosome-lysosome fusion.

Taking advantage of the RNAi lines, we next investigated thoroughly the consequences of lacking glial VAMP7 in the brains. Striking defects were detected

when analyzing Transmission Electron Microscopy (TEM) images of adult fly brains expressing *vamp7*-RNAi in glia. In addition to the presence of LDs and mitophagic vacuoles, mitochondria were elongated, indicating a possible defect in fission or fusion (yellow arrows, Figure 1A). The morphologies of mitochondria were categorized and quantified by comparing the values of mitochondrial length over diameter (L/D). Interestingly, the ratio of mitochondria with a L/D number lower than 2.5 decreased, whereas the ones with a L/D number higher than 2.5 increased upon glial VAMP7 depletion (Figures 1A and 1B). These results indicate that mitochondria exhibit elongated morphology in the absence of glial VAMP7. Furthermore, two independent mitochondrial markers: *UAS-mito-HA-GFP* (*mito.GFP*) and *UAS-mitoOMM-mCherry* (*mitoOMM.mCherry*), that expresses a mitochondrial import signal and labels the outer mitochondrial membrane, respectively, were used to assess glial mitochondrial dynamics in the absence of VAMP7. Consistent with the EM results, mitochondrial area and volume were significantly increased when expressing *vamp7*-RNAi in glia, indicating that mitochondria are elongated (Figures 1C-1E and S1D-S1F). Taken together, these results indicate that lack of glial VAMP7 disrupts mitochondrial dynamics, possibly due to a defect in fission or fusion.

Given that VAMP7 is a characterized fusion factor in autophagy, we next determine if VAMP7-mediated glial mitochondrial dynamics depends on autophagosome-lysosome fusion. Interestingly, mitochondrial area and volume in glia were not altered in the presence of Bafilomycin A1 (BafA1), a drug blocking autophagosome-lysosome fusion (21, 22) (Figures 1F-1H). Moreover, glial inhibition

of the other factor involved in autophagosome-lysosome fusion, Syx17, did not cause mitochondrial elongation (Figures S1G-S1I). Taken together, these results indicate that VAMP7 mediates glial mitochondrial dynamics independent of its function in autophagosome-lysosome fusion.

Lack of glial VAMP7 leads to mitochondrial dysfunction

To further demonstrate that VAMP7-mediated mitochondrial elongation is physiologically relevant, the calcium sensor *mitoGCamp5.0* was expressed in glia to monitor the mitochondrial calcium activity (23). Whereas an increase in the *mitoGCamp5.0* signal was detected in the control young animals, the increase was blocked when silencing glial *vamp7* expression (Figure 2A). The increased *mitoGCamp5.0* signal was similarly blocked by glial VAMP7 depletion when flies aged (Figure 2B). These results indicate that glial VAMP7 regulates mitochondrial calcium activity. As mitochondria are the major sites for ROS production, adult fly brains of control and *repo>vamp7*-RNAi animals were examined for ROS levels with the dihydroethidium (DHE) staining. Consistent with previous findings, DHE-positive fluorescent intensities increased when expressing the RNAi targeting *superoxide dismutase* 1 (*sod1*), the enzyme that regulates ROS levels by catalyzing the conversion of superoxide into oxygen and hydrogen peroxide (Figure 2C). Interestingly, inhibiting *vamp7* expression in glia caused similar increase, indicating that glial VAMP7 expression regulates cellular ROS levels (Figure 2C). In addition, the transcriptional levels of genes related to the mitochondrial fatty acid β-oxidation

pathway, including those encoding acyl-coA dehydrogenases (*CG17544* and *CG9527*) and fatty acid synthase (*FASN*), were increased upon glial *vamp7*-RNAi expression, indicating altered mitochondrial function (24, 25) (Figure 2D). Notably, the levels of BODIPY-positive LDs increased in both larval and adult fly brains in the absence of glial VAMP7 (Figures 2E-2G), with a similar increase in the overall LD triacylglycerols (TAG) content (Figure 2H). The increased LD number was suppressed in the presence of α-Lipoic acid, a compound known for suppressing LD formation (Figures 2I and 2J), indicating that glial VAMP7 regulates LD formation. Taken together, these results indicate that glial VAMP7 regulates mitochondrial function, ROS levels, and LD production via modulating mitochondrial dynamics in glia.

Glial VAMP7 contributes to DA neuron survival

As glia interact with neurons and the glia-neuron crosstalk often contributes to neuronal function and survival, we next investigated if VAMP7-mediated glial mitochondrial dynamics contributes to DA neuron survival using the *Drosophila* PD model established in the lab. DA neurons are located in clusters and named upon their relative positions in adult fly brains (26, 27). These clusters include protocerebral posterior lateral (PPL)1, PPL2, protocerebral posterior medial (PPM)1, PPM2, and PPM3 (Figure 3A). Interestingly, lack of glial VAMP7 causes DA neuron loss at PPM1/2, PPM3, and PPL1 clusters in an age-dependent manner (Figures 3B-3D). These results suggest that glial VAMP7 contributes to DA neuron survival. Given that

the degeneration of DA neurons in the PPM1/2 cluster has been implicated in a *Drosophila* PD model overexpressing α-Synuclein (28), it is conceivable that glial VAMP7 plays important roles in regulating DA neuron survival under pathological conditions.

Glial VAMP7 regulates mitochondrial fission and fusion

Given that lack of glial VAMP7 induces mitochondrial elongation, possibly due to decreased fission or increased fusion, we tested genetically if glial VAMP7 interacts with the fission factor Drp1 or the fusion factor Marf. Interestingly, increased Drp1 expression suppressed the mitochondrial elongation in the absence of glial VAMP7 (Figures 3E-3G), suggesting that increasing fission helps to prevent VAMP7-mediated mitochondrial elongation. Moreover, decreased Marf expression in the presence of glial *vamp7*-RNAi also suppressed the mitochondrial elongation. These results indicate that Drp1 and Marf are epistatically downstream of glial VAMP7 in controlling mitochondrial fission and fusion. Interestingly, endogenous protein levels of Fission, mitochondrial 1 (Fis1), Drp1, Marf, and Optic astrophy 1 (Opa1) were not affected by the absence of glial VAMP7, suggesting that VAMP7 does not regulate glial mitochondrial dynamics via tuning fission/fusion proteins levels (29) (Figures S2A-S2H). These results suggest that glial VAMP7 acts upstream of these mitochondrial factors in regulating mitochondrial fission/fusion; mitochondrial elongation caused by the lack of glial VAMP7 is potentially due to a change in the dynamic or balance of fission and fusion.

Glial VAMP7 regulates the dynamic of mitochondria-lysosome contact

It has been reported that lysosomes contact mitochondria to restrict its motility and determine the fission site (16, 30). Given that VAMP7 is localized on the lysosome, we next investigated whether glial VAMP7 regulates mitochondrial dynamic via the mitochondria-lysosome contact. Two reporters: *UAS-mitoOMM-mCherry* and *UAS-Lamp1-GFP*, were co-expressed to label mitochondria and lysosomes simultaneously, such that mitochondria-lysosome contact can be visualized under various conditions. Interestingly, colocalization of mitoOMM and Lamp1 increased upon glial VAMP7 depletion, indicating an increase in mitochondria-lysosome contact (Figures 4A and 4B). Importantly, these dual positive contacts were not positive for the autophagosome marker Atg8a, indicating that these do not represent mitochondria undergoing mitophagy (Figures S2I-S2K). Whereas the value of Pearson's coefficient for mitoOMM and Lamp1 increased significantly (Figure S2J), the colocalization values for Atg8a and mitoOMM decreased upon glial VAMP7 depletion (Figure S2K). These results indicate that lack of glial VAMP7 increases mitochondria-lysosome contact and blocks mitophagy, consistent with the notion that elongated mitochondria are resistant to and slows down mitophagy.

In addition, the dynamics of colocalized mitoOMM and Lamp1 were analyzed by time lapse analysis *in-vivo*. Interestingly, mitochondria and lysosomes contacted each other and dissociated over a course of 100 seconds, whereas the duration of these contacts persisted and prolonged up to 400 seconds upon glial VAMP7 depletion

(Figures 4C, 4D, and Movie S1-S3). The frequency of mitochondria and lysosome contacting each other and the duration of these contacts increased significantly (Figures 4E and 4F) and a higher number of contacts persisting more than 5 min was also detected (Figure 4G). Consistently, mitochondria and lysosome were significantly less mobile in the absence of glial VAMP7 as indicated by their moving speed (Figures 4H and 4I). Taken together, these results indicate that glial VAMP7 regulates the dynamics of mitochondria-lysosome contacts.

Discussion

SNARE proteins are canonical regulators of membrane fusion, yet to date no evidence indicates that they mediate mitochondrial fusion. Mitochondrial fission, however, has been shown to rely on the activity of SNARE protein Syx17. Upon starvation-induced autophagy, Syx17-Drp1 interaction is disrupted, causing a block in mitochondrial fission, hence the elongated mitochondria resistant to mitophagy (31). Syx17 also mediates fusion between the mitochondrial-derived vesicles (MDVs) and the late endosome/lysosome under stress conditions (32). These results indicate that SNARE proteins are possible mediators in mitochondrial dynamics. *Drosophila* VAMP7 is highly homologous with mammalian VAMP8, which exhibits prominent expression in microglia. Our findings reveal that lack of glial VAMP7 causes elongated mitochondria, a phenotype genetically suppressed by increasing the expression of the fission factor Drp1. These elongated mitochondria are dysfunctional as mitochondrial calcium activity is significantly disrupted and the levels of ROS and

lipid droplets are increased, endangering the survival of nearby DA neurons. Despite a role in autophagosome-lysosome fusion, glial VAMP7-mediated mitochondrial dynamics does not depend on its fusion function as inhibiting autophagosome-lysosome fusion by BafA1 does not alter mitochondrial length.

Mitochondrial fission site is determined by contacts between mitochondria and ER or lysosomes. With its lysosomal localization, it is intriguing to speculate that VAMP7 regulates mitochondria-lysosome contacts, determines the mitochondrial fission site, in turn controls the fate of mitochondria undergoing fission, fusion, or inter-mitochondrial clustering. Multiple lines of evidence support this hypothesis: first, elongated mitochondria were aggregated and exhibit increasing contacts with lysosomes upon glial VAMP7 depletion, suggesting abnormal tethering among mitochondria themselves or between mitochondria and lysosomes. These abnormal clusterings do not represent mitophagy events as no Atg8a-positive autophagosomes are detected at these sites. Rather, the phenomenon suggests defective mitochondria-lysosome contacts, which prevent mitochondria from fission, hence the elongation. Similarly, the critical regulator Rab7 in mitochondria-lysosome contact also appears to be mislocalized and aggregated in the absence of glial VAMP7, further suggesting the disruptive formation of mitochondria-lysosome contact (Figure S3A). It is noteworthy to mention that lysosomes exhibit abnormal acidity in the absence of glial VAMP7 (Figures S3B and S3C). Moreover, as contact sites between mitochondria and ER are known as sites for calcium transfer, inhibiting the glial expression of TRPML, a mucolipin channel on the lysosomal membrane that releases

calcium, does not cause mitochondrial elongation (Figures S3D-S3F). These findings suggest that lysosomal calcium transfer might not be responsible for the persisted contacts and mitochondrial elongation induced by glial VAMP7 depletion. Mitochondria-lysosome contacts might provide a more direct and physical cue to modulate glial mitochondrial dynamics, via a route different from the calcium transfer between mitochondria and ER.

Similar to neurons, glia, particularly astrocytes, possess SNARE machineries for their vesicular trafficking function. These SNARE machineries, some in the same composition as in neurons but some different, are responsible for slow secretory exocytosis rather than fast and immediate release of signaling molecules (33). Very importantly, they regulate synaptic transmission and plasticity, antigen presentation in neuro-inflammation, and control different types of behavior such as sleep. Our findings unexpectedly reveal a new role for the canonical SNARE protein VAMP7 in glial mitochondrial dynamics. Considering that mitochondria are present in astrocytic processes in close proximity to neurons and contribute to local calcium signaling, ATP production, and metabolism of signaling molecules, it is conceivable that VAMP7-mediated glial mitochondrial dynamics subsequently impacts mitochondrial function and participates in the metabolic process supporting neuron survival. Given that DA neurodegeneration is one of the hallmarks in PD, our findings illustrate a SNARE-dependent mechanism controlling organelle contacts, glial mitochondrial dynamics, and DA neuron survival, providing the mechanistic basis underlying DA neurodegeneration. Canonical SNARE proteins not only regulate membrane fusion,

but also important mediators in mitochondrial dynamics; future work is warranted to explore additional roles of SNARE proteins in various cellular contexts in both cell-autonomous and non-cell-autonomous fashions.

Acknowledgements

We thank Bloomington *Drosophila* Stock Center, Vienna *Drosophila* RNAi Center, Tsinghua Fly Center, the Core Facility of *Drosophila* Resource and Technology, Shanghai Institute of Biochemistry and Cell Biology, Chinese Academy of Sciences, Developmental Studies Hybridoma Bank, Chao Tong, Chun-Hong Chen, Henry Sun, and Aike Guo for fly stocks and antibodies. We also thank the Molecular Imaging Core Facility (MICF), the Molecular and Cell Biology Core Facility (MCBCF), and the Multi-Omics Core Facility (MOCF) at the School of Life Science and Technology, ShanghaiTech University for providing technical support; Yu Kong and Lijun Pan in Electron Microscopy Facilities of Center for Excellence in Brain Science and Technology, Chinese Academy of Science for assistance with EM sample preparation. We thank Ho lab members for discussion and comments. This work was supported by grants from ShanghaiTech and National Natural Science Foundation of China (31871039).

Author Contributions

H.W, S.Z, and M.S.H conceived and designed the study. H.W, L.W, and S.Y performed the experiments. H.W and M.S.H analyzed the data. M.S.H wrote the paper

with input from H.W. All authors read and approved the manuscript.

Declaration of Interests

The authors declare no competing interests.

Figure Legends

Figure 1. Lack of glial VAMP7 causes mitochondrial elongation (**A** and **B**) Representative TEM images (A) and quantifications (B) of mitochondrial morphology in control and *repo>vamp7*-RNAi^{43543} adult fly brains of 10-day-old. Note the presence of lipid droplets (red arrows), mitophagic vacuoles (pink arrows), and elongated mitochondria (yellow arrows) in the absence of glial VAMP7. Note that the ratio of mitochondria with a length to diameter (L/D) number lower than 2.5 is significantly lower while the ratio for L/D number above 2.5 is significantly higher upon glial VAMP7 depletion. (**C**-**E**) Representative confocal images (C) and quantifications (D and E) of glial mitochondrial morphology monitored by *UAS-mito.GFP* in control and *repo>vamp7*-RNAi^{43543} adult fly brains. Note that the average mitochondrial area and volume quantified by Imaris are significantly larger than the control animals when expressing *vamp7*-RNAi in glia. (**F**-**H**) Representative confocal images (F) and quantifications (G and H) of glial mitochondrial morphology in the absence or presence of Bafilomycin A1 (BafA1). Note that no change in the mitochondrial area and volume is observed when autophagosome-lysosome fusion is blocked by BafA1. Insets represent enlarged view of single mitochondria. Scale bar:

500 nm in A, 10 μm in C and F. Mitochondrial area and volume are quantified by Imaris as detailed in the Materials and Methods. The numbers of brains analyzed and quantified are indicated in the Figures. For TEM, 6 independent fly brains for each genotype were analyzed. Data are shown as mean ± SEM. P-values of significance (indicated with asterisks, ns no significance, * $p<0.05$, ** $p<0.01$, and *** $p<0.001$) are calculated by two-tailed unpaired t-test. Approximately 20 confocal Z-stack sections were taken with 0.125 μm each. Merged images are shown. All data in subsequent figures are present and analyzed as described above unless stated otherwise.

Figure 2. Lack of glial VAMP7 disrupts mitochondrial function and increases ROS levels and lipid droplet production (**A** and **B**) The reporter *UAS-mitoGCamp5.0* was expressed together with *UAS-mitoOMM.mCherry* in glia to monitor mitochondrial calcium activity (*mitoOMM.mCherry; repo-Gal4, mitoGCamp5.0*). Note that the increased mitochondrial calcium activity is blocked in both young and old flies when inhibiting glial VAMP7 expression. (**C**) DHE fluorescence intensities representing cellular ROS levels were significantly increased upon glial VAMP7 depletion. (**D**) RT-qPCR analysis reveals increased transcription levels of genes related to mitochondrial function including the ones encoding acyl-coA dehydrogenases (*CG17544* and *CG9527*) and fatty acid synthase (*FASN*). (**E-H**) The numbers of LDs labelled by the BODIPY dye in both larval and adult fly brains (E-G) and the TAG content in the LDs (H) are significantly increased in the

absence of glial VAMP7. (**I** and **J**) Glial VAMP7 regulates LD formation as addition of α-lipoic acid suppresses LD formation in both control and *repo>vamp7*-RNAi[43543] adult fly brains of 3-day-old. Scale bar: 100 μm in 3rd instar larvae in E and I, 50 μm in Day 3 in E. The numbers of brains analyzed and quantified are indicated in the Figures. For α-lipoic acid treatment, 8 independent fly brains for each genotype were analyzed. Data are shown as mean ± SEM. P-values of significance (indicated with asterisks, ns no significance, * $p<0.05$, ** $p<0.01$, and *** $p<0.001$) are calculated by two-tailed unpaired t-test.

Figure 3. VAMP7 regulates glial mitochondrial dynamics and DA neuron survival (**A**) An schematic diagram illustrating the DA neuron clusters in adult fly brains. The black dashed box encloses the area visualized in B. (**B**-**D**) The numbers of DA neurons in PPM1/2, PPM3, and PPL1 are significantly decreased (white arrows in B) in the aged flies lacking glial VAMP7. (**E**-**G**) Epistatic analysis of VAMP7 and mitochondrial fission/fusion factors Drp1, Marf, and Opa1 in regulating mitochondrial dynamics. Note that increasing expression of the fission factor Drp1 or downregulating the expression of the fusion factor Marf or Opa1 causes increased fission, opposite to the mitochondrial elongation phenotype in the absence of glial VAMP7. Co-expression of *Drp1*, *Marf*-RNAi, or *Opa1*-RNAi and *vamp7*-RNAi in glia all leads to suppression on mitochondrial elongation. Insets represent enlarged view of single mitochondria. Scale bar: 50 μm in B, 10 μm in E. The numbers of brains analyzed and quantified are indicated in the Figures. For DA neurons statistics,

15 independent fly brains for each genotype were analyzed (C and D). Data are shown as mean ± SEM. P-values of significance (indicated with asterisks, ns no significance, * $p<0.05$, ** $p<0.01$, *** $p<0.001$ and **** $p<0.0001$) are calculated by ordinary one-way ANOVA followed by Tukey's multiple comparisons test.

Figure 4. VAMP7 regulate glial mitochondrial dynamics via mitochondria-lysosome contacts (**A** and **B**) Two reporters *UAS-mitoOMM.mCherry* (labels the mitochondrial outer membrane, red) and *UAS-Lamp1* (labels lysosome, green) are co-expressed to visualize mitochondria-lysosome contact. Note that significant increase in colocalization of mitoOMM and Lamp1 upon glial VAMP7 depletion analyzed by Imaris. Co-localization traces are illustrated in yellow in A. (**C-I**) Representative images (C and D) and quantifications (E-I) of the dynamic of mitochondria-lysosome contact monitored by *in-vivo* time lapse analysis. Note that mitochondria and lysosome contact each other and separate within the course of 100 seconds, while the contact persists up to 400 seconds upon glial VAMP7 depletion. Both the frequency and the duration of the contacts increase, while the mobility of both organelles decrease, when lacking glial VAMP7. Parameters in E-I are quantified using Imaris and ImageJ. Scale bar: 10 μm in A, 5 μm in A (colocalization panel), 1 μm in C and D. The numbers of brains analyzed and quantified are indicated in the Figures. For Lamp1.GFP and mitoOMM.mCherry colocalization statistics, 9 independent fly brains for each genotype were analyzed (B). Data are shown as mean ± SEM. P-values of significance (indicated with asterisks, ns no significance, *

p<0.05, ** p<0.01, and *** p<0.001) are calculated by two-tailed unpaired t-test.

Figure S1. Glia deficient of VAMP7 exhibit mitochondrial elongation (**A**) RT-qPCR analysis indicates that expression of either *vamp7*-RNAi, #38300 or #43543, in glia reduces the *vamp7* transcription levels significantly. (**B** and **C**) Glial autophagic flux monitored by the dual reporter *UAS-GFP-mCherry-Atg8a* is impaired upon glial VAMP7 depletion, suggesting impaired fusion. Note that the Pearson's coefficient value indicating colocalization of GFP and mCherry increases when lacking glial VAMP7 (B). (**D**-**F**) Glial mitochondrial dynamic is monitored by expressing the reporter *UAS-mitoOMM.mCherry* in glia. Consistent with the other reporter *UAS-mito.GFP*, Imaris analysis reveals an increase in the mitochondrial area and volume in the absence of glial VAMP7. (**G**-**I**) Glial inhibition of *syx17* expression does not cause mitochondrial elongation. Note that mitochondrial area and volume quantified using the reporter *UAS-mito.GFP* remain unaffected in the presence of *syx17*-RNAi. Scale bar: 10 μm in C, D and G. Mitochondrial area and volume are quantified by Imaris as detailed in the Materials and Methods. The numbers of brains analyzed and quantified are indicated in the Figures. Data are shown as mean ± SEM. P-values of significance (indicated with asterisks, ns no significance, * p<0.05, ** p<0.01, and *** p<0.001) are calculated by two-tailed unpaired t-test or ordinary one-way ANOVA followed by Tukey's multiple comparisons test. Approximately 20 confocal Z-stack sections were taken with 0.125 μm each. Merged images are shown. All data in subsequent figures are present and analyzed as described above unless

stated otherwise.

Figure S2. VAMP7 regulates glial mitochondrial dynamics via mitochondria-lysosome contact (**A**-**H**) Western blot analysis of endogenous fission/fusion protein levels in the control and *repo>vamp7*-RNAi animals. Knock-in lines at the original locus of Drp1, Opa1, and Marf created with an insertion of the HA tag for protein detection and the Fis1 antibodies are gifts from Chun-Hong Chen. (**I**-**K**) Two reporters *UAS-mitoOMM.mCherry* (labels the mitochondrial outer membrane, red) and *UAS-Lamp1* (labels lysosome, green) are co-expressed to visualize mitochondria-lysosome contact. Note that significant increase in colocalization of mitoOMM and Lamp1 upon glial VAMP7 depletion analyzed by Imaris (J). Immunostaining with anti-Atg8a antibodies reveals a decrease in the colocalization of Atg8a and mitoOMM, suggesting that mitophagy is not induced (K). Note that no Atg8a signals are detected in contact puncta positive for mitoOMM and Lamp1 (insets in I). Scale bar: 10 μm in I. The numbers of brains analyzed and quantified are indicated in the Figures. Data are shown as mean ± SEM. P-values of significance (indicated with asterisks, ns no significance, * $p<0.05$, ** $p<0.01$, and *** $p<0.001$) are calculated by two-tailed unpaired t-test or ordinary one-way ANOVA followed by Tukey's multiple comparisons test.

Figure S3. VAMP7 regulates the dynamic of mitochondria-lysosome contact (**A**) Two reporters *UAS-mitoOMM.mCherry* (labels the mitochondrial outer membrane,

red) and *UAS-Rab7.GFP* (labels late endosome and lysosome, green) are co-expressed to visualize the dynamic of Rab7 contacting mitochondria. Note that Rab7 exhibit aggregated and mislocalized pattern upon glial VAMP7 depletion. (**B** and **C**) Lysosomal acidity monitored by the LysoTracker Red dye is significantly impaired when expressing *vamp7*-RNAi in glia. Note that LysoTracker Red fluorescent intensities increase upon glial VAMP7 depletion. (**D**-**F**) Mitochondrial dynamic monitored by the reporter *UAS-mito.GFP* is significantly affected by *trpml*-RNAi expression in glia. Note that mitochondrial area and volume are reduced, indicating rounder and shorter morphology, opposite to mitochondrial elongation. Scale bar: 10 μm in A, B and D. The numbers of brains analyzed and quantified are indicated in the Figures. Data are shown as mean ± SEM. P-values of significance (indicated with asterisks, ns no significance, * $p<0.05$, ** $p<0.01$, and *** $p<0.001$) are calculated by two-tailed unpaired t-test or ordinary one-way ANOVA followed by Tukey's multiple comparisons test.

Movie S1. *In-vivo* time lapse analysis of mitochondria-lysosome contact in the control flies. Two reporters *UAS-mitoOMM.mCherry* (labels the mitochondrial outer membrane, red) and *UAS-Lamp1* (labels lysosome, green) are co-expressed to visualize mitochondria-lysosome contact. A representative contact is shown. A Z-stack of 10 images was taken at an interval of 19 seconds for 10 minutes. Note that mitochondria and lysosomes contact and dissociate over the imaging period.

Movie S2. *In-vivo* time lapse analysis of mitochondria-lysosome contact in flies lacking glial VAMP7. Two reporters *UAS-mitoOMM.mCherry* (labels the mitochondrial outer membrane, red) and *UAS-Lamp1* (labels lysosome, green) are co-expressed to visualize mitochondria-lysosome contact. A representative contact is shown. A Z-stack of 10 images was taken at an interval of 19 seconds for 10 minutes. Note the significant increase in colocalization of mitoOMM and Lamp1 upon glial VAMP7 depletion.

Movie S3. *In-vivo* time lapse analysis of mitochondria-lysosome contact in flies lacking glial VAMP7. Two reporters *UAS-mitoOMM.mCherry* (labels the mitochondrial outer membrane, red) and *UAS-Lamp1* (labels lysosome, green) are co-expressed to visualize mitochondria-lysosome contact. A representative contact different from Movie S2 is shown. A Z-stack of 10 images was taken at an interval of 19 seconds for 10 minutes. Note the significant increase in colocalization of mitoOMM and Lamp1 upon glial VAMP7 depletion.

Materials and Methods

Drosophila genetics

Flies were raised under standard conditions at 25□ with 70% humidity. All fly crosses were carried out at 25°C with standard laboratory conditions unless noted otherwise. All strains were obtained from Bloomington Drosophila Stock Center (BDSC), the Vienna Drosophila RNAi Center (VDRC), Tsinghua Fly Center, or as gifts from

colleagues. The following fly strains were used in this study: *repo-GAL4* (a pan-glial driver), *UAS-luciferase-IR* (BL31603), *UAS-lacZ* (BL1777), *UAS-mito-HA-GFP* (BL8442), *UAS-mito.OMM.mCherry* (BL66532), *UAS-Lamp1.GFP*, *UAS-vamp7 RNAi* (BL38300 and BL43543), *UAS-marf RNAi* (BL31157), *UAS-opa1 RNAi* (THU0811), *UAS-sod1 RNAi* (THU3207), *UAS-Rab7.GFP* (BL42705); *UASp-GFP-mCherry-Atg8a* (Henry Sun); *UAS-HRP* (Aike Guo); *UAS-drp1* (Chao Tong); *drp1-HA*, *opa1-HA*, and *marf-HA* (Chun-Hong Chen).

Molecular biology

qRT-PCR: Total RNAs were extracted from adult fly heads using TransZol Up (Cat. #ET111-01, TransGen, Beijing, China). cDNAs were reversely transcribed using HiScript III RT SuperMix (Cat. #R323-01, Vazyme, Nanjing, China). qRT-PCR reactions were performed using ChamQ Universal SYBR qPCR Master Mix (Cat. #Q711-02, Vazyme) and ABI 7500 RT-PCR system. The mRNA levels were normalized to *rp49* , respectively. The expression levels were analyzed by ΔΔCT method. Primers used for amplification:

rp49-F: CCACCAGTCGGATCGATATGC

rp49-R: CTCTTGAGAACGCAGGCGACC

vamp7-F: GGCTCGCAATTGGATAGTAGT

vamp7-R: TGCTTATCGGGGAATGAGCC

CG17544-F: *GTACTATGCTCTGACGCGCT*

CG17544-R: *GGTGGTCATGTGCTTCTCCA*

CG9527-F*: CTGCTTCCCCTGCTGAAGAA*

CG9527-R*: GACGTTTCCATCGCTCATGC*

FASN-F: *CGCTCCACTCCAAGAACTCG*

FASN-R*: CAGGTTTAGTTGTAGGGGCTAGA*

Immunohistochemistry

Adult fly brains were dissected and fixed in 4% formaldehyde for 45 minutes, then washed with PBT (PBS + 0.3% TX-100) for 3 times and dissected further to remove additional debris in PBS solution. Clean and fixed brains were blocked in PBT solution with 5% Normal Donkey Serum (NDS) or 10% Bovine Serum Albumin (BSA) and subsequently stained with primary antibodies at 4□ overnight and then secondary antibodies at room temperature for 2 hours. Primary antibodies used: mouse anti-Atg8a (1:1000, gift from Chao Tong) and rabbit anti-TH (1:1000, Cat. #NB300-109, Novus). For all samples, secondary antibodies used were from Jackson ImmunoResearch (West Grove, PA, USA): donkey anti-rabbit Cy3 (1:1000, Cat. #711-166-152), donkey anti-mouse Cy5 (1:500, Cat. #715-175-150). All samples were mounted in Vectashield mounting media (Cat. #H-1500-10, Vector Laboratories, Burlingame, CA, USA).

***In-vivo* time lapse analysis**

Live adult fly brains were dissected and kept in PBS solution. All samples were mounted in PBS, and immediately scanned anteriorly to posteriorly (top to bottom) using Nikon C2 confocal microscope (Tokyo, Japan) with a 60X oil objective. The

number of contacts were analyzed by Imaris using Autoregressive motion tracking mode. Duration of contacts were analyzed by ImageJ using Time stamper.

Calcium imaging

Live adult fly brains expressing mitoGCamp5.0 were dissected and kept in PBS solution. All samples were mounted in PBS, and immediately scanned in a single focal plane using Nikon A1 confocal microscope (Tokyo, Japan) with a 60X oil objective. The fluorescence intensity were analyzed by ImageJ using Time series analyzer V3.

Live fluorescent dye imaging

Live adult fly brains were dissected and kept in PBS solution. For the analysis of LDs, brains were incubated with 1 μg/mL BODIPY™ 493/503 (Cat. #D3922, Invitrogen) for 5 minutes at 25°C, then immediately scanned by the Nikon C2 confocal microscope (Tokyo, Japan) with a 20X objective. To analyze LD formation, brains were also treated with 10 μM α-Lipoic acid (Cat #D118666, Aladdin) for 3 days, followed by 1 μg/mL BODIPY™ 493/503 (Cat. #D3922, Invitrogen) for 5 minutes at 25°C, then immediately scanned by the Nikon C2 confocal microscope (Tokyo, Japan) with a 20X objective. For the analysis of mitochondria-derived ROS levels, brains were incubated with 5 μM DHE (Cat. #D11347, Invitrogen) for 5 minutes at 25°C, then immediately scanned using the Nikon A1 confocal microscope (Tokyo, Japan) with a 20X objective. For the analysis of lysosome acidity, brains

were incubated with LysoTracker Red DND-99 (1:1000, Cat. #40739ES50, Yeasen) solution in PBS for 5 minutes at 25°C, then immediately scanned using Nikon C2 confocal microscope (Tokyo, Japan) with a 60X oil objective.

Transmission electron microscopy

Adult fly brains were fixed, embedded, stained, and dehydrated according to previous protocols (34). Ultrathin sections (70 nm) of each brain were cut with a Diatomediamond knife on a Leica EM UC7 ultra-microtome (Leica Microsystems, Germany) and collected on copper grids. Images were acquired with Talos L120C transmission electron microscope (Thermo Fisher Scientific, Waltham, MA, UAS) operating at an acceleration voltage of 120 kV.

Biochemistry

Adult fly heads were homogenised using a motorised pestle (Cat. #116005500, MP Biomedicals, Irvine, CA, USA) in lysis buffer (0.4% NP-40, 0.2 mM EDTA, 150 mM NaCl, 20% glycerol, 100 mM Tris-HCl pH7.5, 2% Tween 20, 0.5 mM phosphodiesterase inhibitors, and 1 mM PMSF). Proteins were separated on SDS-PAGE gels and transferred to PVDF membranes (Cat. #IPFL00010, Millipore, Billerica, MA, USA). The membranes were blocked by 5% fat-free milk diluted in PBS with 0.1% Tween-20 for 40 minutes. Samples were incubated with the primary antibodies at 4°C overnight and HRP-conjugated secondary antibodies at room temperature for 2 hours. Primary antibodies used: rat anti-HA-HRP (1:1000, Cat.

#3F10, Roche), mouse anti-α-Tubulin (1:5000, Cat. #T9026, Sigma). Bands were visualized by Clarity Western ECL Substrate (Cat. #WBKLS0500, Millipore). Results are representative of at least three biological replicates. For BafilomycinA1 treatment: BafA1 (Cat. #BML-CM110-0100, ENZO) was diluted in DMSO (Cat. #D8371-50, solarbio) in a concentration of 1 mM, then added to 0.5 ml of liquid yeast for a final concentration of 4 μM. Yeast containing BafA1 was added to the top of the fly food in standard vials kept overnight to allow the evaporation of residual DMSO. Flies of different genotypes (20 females and 20 males) were then put in each vial and kept at 25°C for 5 days. After treatment, flies were collected for western blot analysis. The TAG content in the LD was quantified by an triglyceride assay kit (Cat #E1103, Applygen Technologies).

Confocal microscopy and statistical analysis

Images of adult fly brains were acquired by scanning a serial Z-stack of average 10-20 sections, each of 0.8 or 0.125 μm thickness, using Nikon A1, C2 confocal microscope (Tokyo, Japan) with the 20X or 60X oil objective. The whole brain was positioned so that they can be scanned anteriorly to posteriorly (top to bottom). For statistical analyses of mitochondrial area and volume, original and unmodified images were imported into Imaris 9.6 (Oxford Instruments) using Surface to create parameters to batch data from different sample groups. For statistical analyses of LD number and intensity, original and unmodified images were imported into ImageJ (National Institutes of Health), and the intensity threshold for the relevant channel was set so

that maximum number of dots were selected without miscounting two adjacent dots into one. For colocalization measurements, primary images were imported into ImageJ (National Institutes of Health) or Imaris 9.6 (Oxford Instruments), and analyzed automatically using the colocalization plugin with the intensity correlation tool, showing as Pearson's correlation coefficient (R) or colocalized trace. All data were imported into GraphPad Prism 7 and shown in scatter plots or column bar graphs. For calculating the statistical significance, two-tailed unpaired t-test or ordinary one-way ANOVA followed by Tukey's multiple comparisons test was used. P value less than 0.05 is considered significant. ns: no significance, $p \geq 0.05$; *: $p<0.05$; **: $p<0.01$; ***: $p<0.001$; ****: $p<0.0001$.

References

1. A. R. Fenton, T. A. Jongens, E. L. F. Holzbaur, Mitochondrial dynamics: Shaping and remodeling an organelle network. *Curr Opin Cell Biol* **68**, 28-36 (2020).
2. S. Gao, J. Hu, Mitochondrial Fusion: The Machineries In and Out. *Trends Cell Biol* **31**, 62-74 (2021).
3. S. Mattie, M. Krols, H. M. McBride, The enigma of an interconnected mitochondrial reticulum: new insights into mitochondrial fusion. *Curr Opin Cell Biol* **59**, 159-166 (2019).
4. D. H. Cho, T. Nakamura, S. A. Lipton, Mitochondrial dynamics in cell death and neurodegeneration. *Cell Mol Life Sci* **67**, 3435-3447 (2010).
5. K. Itoh, K. Nakamura, M. Iijima, H. Sesaki, Mitochondrial dynamics in neurodegeneration. *Trends Cell Biol* **23**, 64-71 (2013).
6. J. R. Friedman *et al.*, ER tubules mark sites of mitochondrial division. *Science* **334**, 358-362 (2011).
7. R. Kalia *et al.*, Structural basis of mitochondrial receptor binding and constriction by DRP1. *Nature* **558**, 401-405 (2018).
8. S. C. Kamerkar, F. Kraus, A. J. Sharpe, T. J. Pucadyil, M. T. Ryan, Dynamin-related protein 1 has membrane constricting and severing abilities sufficient for mitochondrial and peroxisomal fission. *Nat Commun* **9**, 5239 (2018).

9. H. Otera *et al.*, Mff is an essential factor for mitochondrial recruitment of Drp1 during mitochondrial fission in mammalian cells. *J Cell Biol* **191**, 1141-1158 (2010).
10. C. S. Palmer *et al.*, Adaptor proteins MiD49 and MiD51 can act independently of Mff and Fis1 in Drp1 recruitment and are specific for mitochondrial fission. *J Biol Chem* **288**, 27584-27593 (2013).
11. Y. Kageyama *et al.*, Mitochondrial division ensures the survival of postmitotic neurons by suppressing oxidative damage. *J Cell Biol* **197**, 535-551 (2012).
12. M. E. Gegg *et al.*, Mitofusin 1 and mitofusin 2 are ubiquitinated in a PINK1/parkin-dependent manner upon induction of mitophagy. *Hum Mol Genet* **19**, 4861-4870 (2010).
13. A. Tanaka *et al.*, Proteasome and p97 mediate mitophagy and degradation of mitofusins induced by Parkin. *J Cell Biol* **191**, 1367-1380 (2010).
14. E. Ziviani, R. N. Tao, A. J. Whitworth, Drosophila parkin requires PINK1 for mitochondrial translocation and ubiquitinates mitofusin. *Proc Natl Acad Sci U S A* **107**, 5018-5023 (2010).
15. Y. C. Wong, W. Peng, D. Krainc, Lysosomal Regulation of Inter-mitochondrial Contact Fate and Motility in Charcot-Marie-Tooth Type 2. *Dev Cell* **50**, 339-354 e334 (2019).
16. Y. C. Wong, D. Ysselstein, D. Krainc, Mitochondria-lysosome contacts regulate mitochondrial fission via RAB7 GTP hydrolysis. *Nature* **554**, 382-386 (2018).
17. Y. Zhang *et al.*, An RNA-sequencing transcriptome and splicing database of glia, neurons, and vascular cells of the cerebral cortex. *J Neurosci* **34**, 11929-11947 (2014).
18. Y. Zhang *et al.*, Purification and Characterization of Progenitor and Mature Human Astrocytes Reveals Transcriptional and Functional Differences with Mouse. *Neuron* **89**, 37-53 (2016).
19. W. Hong, SNAREs and traffic. *Biochim Biophys Acta* **1744**, 120-144 (2005).
20. X. Tian, J. Teng, J. Chen, New insights regarding SNARE proteins in autophagosome-lysosome fusion. *Autophagy* 10.1080/15548627.2020.1823124, 1-9 (2020).
21. C. Mauvezin, P. Nagy, G. Juhasz, T. P. Neufeld, Autophagosome-lysosome fusion is independent of V-ATPase-mediated acidification. *Nat Commun* **6**, 7007 (2015).
22. T. Yoshimori, A. Yamamoto, Y. Moriyama, M. Futai, Y. Tashiro, Bafilomycin A1, a specific inhibitor of vacuolar-type H(+)-ATPase, inhibits acidification and protein degradation in lysosomes of cultured cells. *J Biol Chem* **266**, 17707-17712 (1991).
23. G. A. Smith *et al.*, Glutathione S-Transferase Regulates Mitochondrial Populations in Axons through Increased Glutathione Oxidation. *Neuron* **103**, 52-65 e56 (2019).
24. Y. Liu, H. Bao, W. Wang, H. Y. Lim, Cardiac Snail family of transcription factors directs systemic lipid metabolism in Drosophila. *PLoS Genet* **15**,

e1008487 (2019).

25. R. Senos Demarco, B. S. Uyemura, C. D'Alterio, D. L. Jones, Mitochondrial fusion regulates lipid homeostasis and stem cell maintenance in the Drosophila testis. *Nat Cell Biol* **21**, 710-720 (2019).

26. V. Budnik, K. White, Catecholamine-containing neurons in Drosophila melanogaster: distribution and development. *J Comp Neurol* **268**, 400-413 (1988).

27. D. R. Nassel, K. Elekes, Aminergic neurons in the brain of blowflies and Drosophila: dopamine- and tyrosine hydroxylase-immunoreactive neurons and their relationship with putative histaminergic neurons. *Cell Tissue Res* **267**, 147-167 (1992).

28. M. B. Feany, W. W. Bender, A Drosophila model of Parkinson's disease. *Nature* **404**, 394-398 (2000).

29. P. L. Chen *et al.*, Vesicular transport mediates the uptake of cytoplasmic proteins into mitochondria in Drosophila melanogaster. *Nat Commun* **11**, 2592 (2020).

30. C. M. Deus, K. F. Yambire, P. J. Oliveira, N. Raimundo, Mitochondria-Lysosome Crosstalk: From Physiology to Neurodegeneration. *Trends Mol Med* **26**, 71-88 (2020).

31. K. Arasaki *et al.*, A role for the ancient SNARE syntaxin 17 in regulating mitochondrial division. *Dev Cell* **32**, 304-317 (2015).

32. G. L. McLelland, S. A. Lee, H. M. McBride, E. A. Fon, Syntaxin-17 delivers PINK1/parkin-dependent mitochondrial vesicles to the endolysosomal system. *J Cell Biol* **214**, 275-291 (2016).

33. A. Verkhratsky, M. Matteoli, V. Parpura, J. P. Mothet, R. Zorec, Astrocytes as secretory cells of the central nervous system: idiosyncrasies of vesicular secretion. *EMBO J* **35**, 239-257 (2016).

34. H. Li, Y. Li, Z. Lei, K. Wang, A. Guo, Transformation of odor selectivity from projection neurons to single mushroom body neurons mapped with dual-color calcium imaging. *Proc Natl Acad Sci U S A* **110**, 12084-12089 (2013).

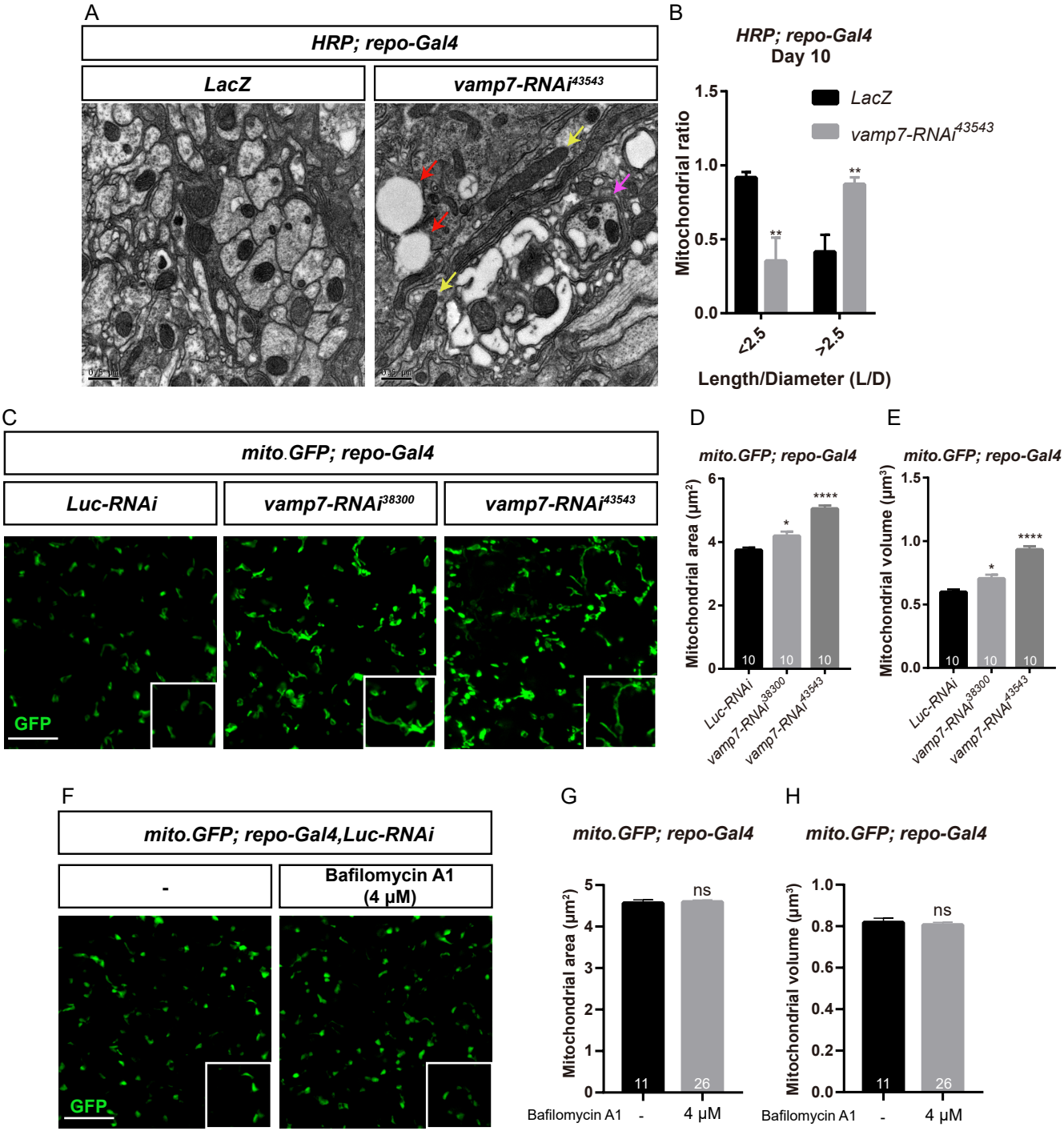
A
HRP; repo-Gal4
LacZ
vamp7-RNAi43543
B
HRP; repo-Gal4
Day 10
LacZ
vamp7-RNAi43543
Mitochondrial ratio
1.5
1.0
0.5
0.0
**
**
<2.5
>2.5
Length/Diameter (L/D)
C
mito.GFP; repo-Gal4
Luc-RNAi
vamp7-RNAi38300
vamp7-RNAi43543
GFP
D
mito.GFP; repo-Gal4
Mitochondrial area (µm²)
6
4
2
0
*
****
10
10
10
Luc-RNAi
vamp7-RNAi38300
vamp7-RNAi43543
E
mito.GFP; repo-Gal4
Mitochondrial volume (µm³)
1.5
1.0
0.5
0.0
*
****
10
10
10
Luc-RNAi
vamp7-RNAi38300
vamp7-RNAi43543
F
mito.GFP; repo-Gal4,Luc-RNAi
-
Bafilomycin A1
(4 µM)
GFP
G
mito.GFP; repo-Gal4
Mitochondrial area (µm²)
5
4
3
2
1
0
ns
11
26
Bafilomycin A1
-
4 µM
H
mito.GFP; repo-Gal4
Mitochondrial volume (µm³)
1.0
0.8
0.6
0.4
0.2
0.0
ns
11
26
Bafilomycin A1
-
4 µM

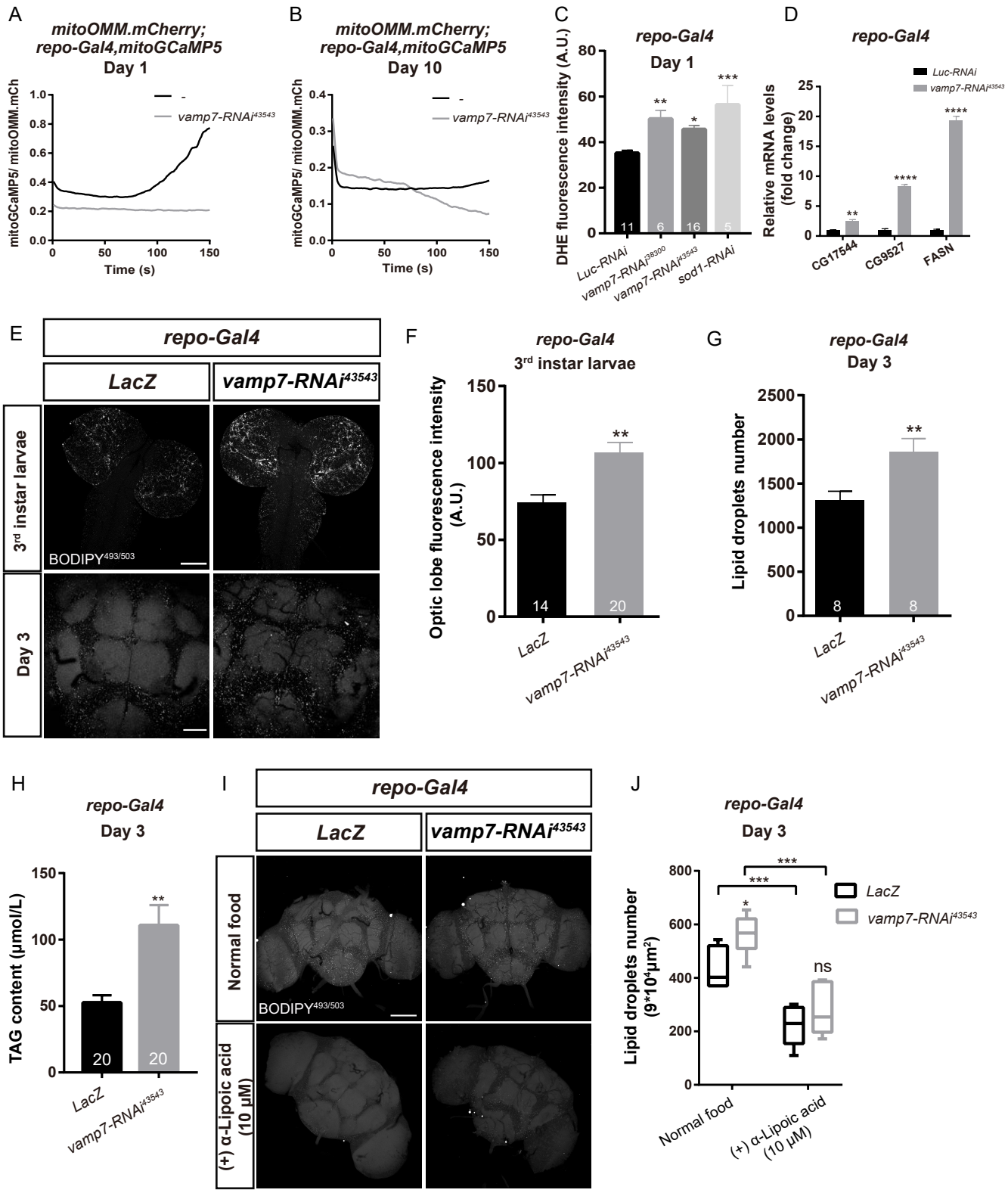
A
mitoOMM.mCherry;
repo-Gal4,mitoGCaMP5
Day 1
mitoGCaMP5/ mitoOMM.mCh
Time (s)
-
vamp7-RNAi43543
B
mitoOMM.mCherry;
repo-Gal4,mitoGCaMP5
Day 10
mitoGCaMP5/ mitoOMM.mCh
Time (s)
-
vamp7-RNAi43543
C
repo-Gal4
Day 1
DHE fluorescence intensity (A.U.)
11
6
16
5
Luc-RNAi
vamp7-RNAi38300
vamp7-RNAi43543
sod1-RNAi
D
repo-Gal4
Relative mRNA levels (fold change)
Luc-RNAi
vamp7-RNAi43543
CG17544
CG9527
FASN
E
repo-Gal4
LacZ
vamp7-RNAi43543
3rd instar larvae
Day 3
BODIPY493/503
F
repo-Gal4
3rd instar larvae
Optic lobe fluorescence intensity (A.U.)
14
20
LacZ
vamp7-RNAi43543
G
repo-Gal4
Day 3
Lipid droplets number
8
8
LacZ
vamp7-RNAi43543
H
repo-Gal4
Day 3
TAG content (µmol/L)
20
20
LacZ
vamp7-RNAi43543
I
repo-Gal4
LacZ
vamp7-RNAi43543
Normal food
(+) α-Lipoic acid (10 µM)
BODIPY493/503
J
repo-Gal4
Day 3
Lipid droplets number (9*10⁴µm²)
LacZ
vamp7-RNAi43543
ns
Normal food
(+) α-Lipoic acid (10 µM)

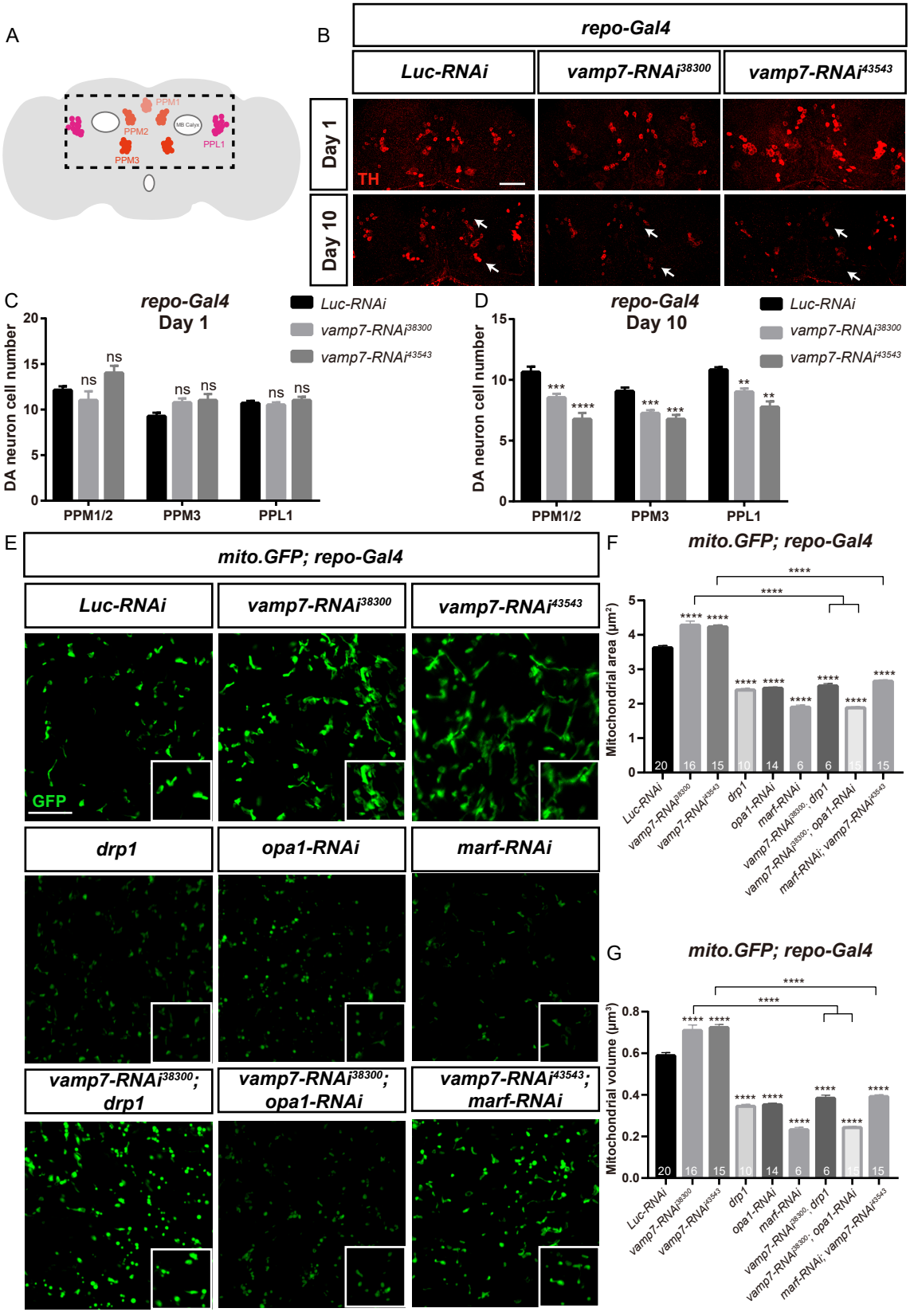
A
PPM1
PPM2
MB Calyx
PPL1
PPM3
B
repo-Gal4
Luc-RNAi
vamp7-RNAi38300
vamp7-RNAi43543
Day 1
Day 10
TH
C
repo-Gal4
Day 1
Luc-RNAi
vamp7-RNAi38300
vamp7-RNAi43543
DA neuron cell number
ns
PPM1/2
PPM3
PPL1
D
repo-Gal4
Day 10
Luc-RNAi
vamp7-RNAi38300
vamp7-RNAi43543
DA neuron cell number
***
****
**
PPM1/2
PPM3
PPL1
E
mito.GFP; repo-Gal4
Luc-RNAi
vamp7-RNAi38300
vamp7-RNAi43543
GFP
drp1
opa1-RNAi
marf-RNAi
vamp7-RNAi38300; drp1
vamp7-RNAi38300; opa1-RNAi
vamp7-RNAi43543; marf-RNAi
F
mito.GFP; repo-Gal4
Mitochondrial area (µm²)
****
20
16
15
10
14
6
6
15
15
Luc-RNAi
vamp7-RNAi38300
vamp7-RNAi43543
drp1
opa1-RNAi
marf-RNAi
vamp7-RNAi38300; drp1
vamp7-RNAi38300; opa1-RNAi
marf-RNAi; vamp7-RNAi43543
G
mito.GFP; repo-Gal4
Mitochondrial volume (µm³)
****
20
16
15
10
14
6
6
15
15
Luc-RNAi
vamp7-RNAi38300
vamp7-RNAi43543
drp1
opa1-RNAi
marf-RNAi
vamp7-RNAi38300; drp1
vamp7-RNAi38300; opa1-RNAi
marf-RNAi; vamp7-RNAi43543

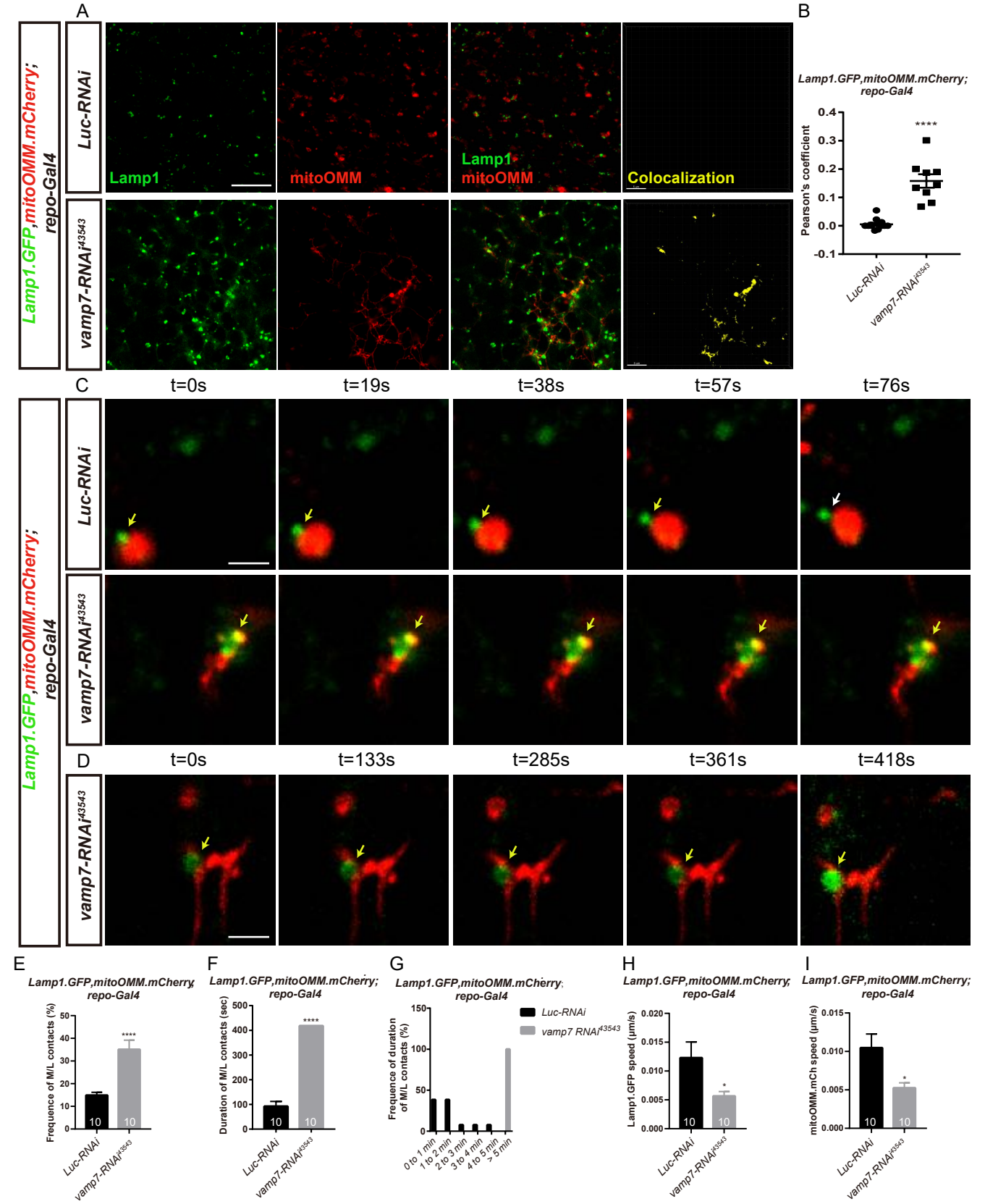
A
Lamp1.GFP,mitoOMM.mCherry; repo-Gal4
Luc-RNAi
vamp7-RNAi43543
Lamp1
mitoOMM
Lamp1 mitoOMM
Colocalization
B
Lamp1.GFP,mitoOMM.mCherry; repo-Gal4
Pearson's coefficient
****
Luc-RNAi
vamp7-RNAi43543
C
t=0s
t=19s
t=38s
t=57s
t=76s
D
t=0s
t=133s
t=285s
t=361s
t=418s
E
Lamp1.GFP,mitoOMM.mCherry; repo-Gal4
Frequence of M/L contacts (%)
F
Lamp1.GFP,mitoOMM.mCherry; repo-Gal4
Duration of M/L contacts (sec)
G
Lamp1.GFP,mitoOMM.mCherry; repo-Gal4
Frequence of duration of M/L contacts (%)
Luc-RNAi
vamp7 RNAi43543
0 to 1 min
1 to 2 min
2 to 3 min
3 to 4 min
4 to 5 min
> 5 min
H
Lamp1.GFP,mitoOMM.mCherry; repo-Gal4
Lamp1.GFP speed (µm/s)
I
Lamp1.GFP,mitoOMM.mCherry; repo-Gal4
mitoOMM.mCh speed (µm/s)